Chaotic scattering in reactive collisions: A classical analysis

Zoltán Kovács[*][†]

Instituut voor Theoretische Fysica, Universiteit van Amsterdam,
Valckenierstraat 65, NL-1018 XE Amsterdam, The Netherlands

Laurent Wiesenfeld

Laboratoire de Spectrométrie Physique, Université Joseph-Fourier-Grenoble,
Boîte Postale 87, F-38402 Saint-Martin-d'Hères Cédex, France

The method of classical trajectories is used to model indirect reactive collisions of three collinear atoms. A very simple yet representative potential is considered: two kinematically coupled Morse potentials. The collision process displays chaotic scattering in the whole range of energy of interest. This transient chaos is studied in detail through a hierarchic analysis of the singularities of the time delay function. A ternary organization is found in the set of scattering trajectories built on a similar structure of the nonattracting chaotic set of bounded orbits. The origin of the ternary structure is explained in terms of simple periodic orbits and their invariant manifolds. Tools of the thermodynamical formalism are used to extract global quantities characterizing the scattering process. The implications of our findings from the point of view of chemical reactivity studies are also discussed.

PACS number(s): 05.45.+b, 34.10.+x

I. INTRODUCTION

We shall analyze in this paper a chemically reactive collision from the standpoint of classical chaotic scattering theory. It has been known for a long time that classical models for chemical reactions exhibit chaos, in its dynamical sense [1]. It has also been suspected for a long time that the mixing properties of chaotic dynamics might explain some statistical laws observed in unimolecular reactions (half collisions) [2]. In this paper, we do not want to elaborate on general schemes but rather focus on a very simple yet representative example in order to show that chemical reaction models may be analyzed thoroughly by means of chaotic scattering. Consequently it will be possible to give a quantitative description of the particular chaos observed as well as justifications for the study of the role of chaotic scattering in the *quantum* description of chemically relevant systems. We thus find it useful to introduce the subject from two points of view: the standpoints of chemical physics and classical mechanics.

While the classical approach has been pursued earlier by a number of authors, it has been somewhat dormant more recently. Nowadays, owing to the formalization of chaotic scattering theory (for a recent review, see Ref. [3] and references therein), classical trajectory models of re-

activity rest on firmer ground and are actively studied again from this point of view [4-8].

A. Chemical physics standpoint

Many models have been proposed and examined in great detail in order to study reactive collisions like the one we will investigate here: $A+BC \leftrightarrow ABC \leftrightarrow AB+C$, where A, B, and C are symbols for single atoms. It is not our purpose to review those models critically in any way [9]; we just describe here cursorily the approximations that may lead to a model as simple as the one we will use.

Nearly all attempts to analyze reaction probabilities are based on the Born-Oppenheimer approximation (apart from some exceptional configurations such as Jahn-Teller effects or potential surface crossings; see Refs. [10,11]). Separating the rapid motion of the electrons from the slower motion of the nuclei or of the atom as a whole, it leads to eigenenergies $U_i(\mathbf{R})$ depending first on the nuclear coordinates, denoted here collectively by $\mathbf{R}$, and second on the quantized electronic states indexed by i. These energy sheets serve as potential energies in the nuclear Schrödinger equation; the model potential we will use in our classical approach is thought to represent one of them.

These potential surfaces exist in a configuration space of dimension $3N - 6$ for a general molecule of N atoms ($N > 2$). For $N = 3$ or 4 already, solving the nuclear Schrödinger equation is a formidable numerical problem. Consequently, for many years, the semiclassical or classical formalisms have seemed to be very attractive in order to calculate reaction probabilities more easily because of the enormous difference, in practice, between the partial

---

[*]On leave from the Institute for Theoretical Physics, Eötvös University, Budapest.

[†]Also at Laboratoire de Spectrométrie Physique, Université Joseph-Fourier-Grenoble, F-38402 Saint-Martin-d'Hères Cedex, France.

differential equations of quantum mechanics and the ordinary differential equations of classical mechanics [12–14].

Chaotic scattering has been discovered experimentally in the Ericson fluctuations of nuclear physics [15]. Several kinds of experiments on waves have demonstrated the validity of the ideas of *quantum* chaotic scattering [16,17]. Another justification for studying classical models, which is our main point, is the existence of matrix elements $S_{vv' JJ'}(E)$ wildly oscillating with E [7]. The reaction particularly studied in this respect was collinear: C + NO $\leftrightarrow$ CNO $\leftrightarrow$ CN + O, a reaction of importance in combustion after-processes.

From an experimental point of view, it makes sense to consider a collinear model with a two-dimensional configuration space [18,19]. The potential used for the analysis was of the type called PQLEPS [18], showing a deep hole in the CNO region. Indications of quantum chaotic scattering are latent in these calculations. Also, preliminary studies have shown that classical chaos occurs, although no characterization was attempted. These results on a potential of no prominent specificity are the main incentives that lead us to the study presented here. We have chosen to simplify the problem at hand by using two coupled Morse potentials (see Sec. II). These potentials retain enough features of the more flexible PQLEPS potentials to show effectively chaotic classical scattering and yet are simple enough to allow for large scale classical calculations.

B. Classical mechanics standpoint

Although classical chaos is now a well established branch of dynamics, its analysis has long been restrained to bound systems where a representative point stays forever on the chaotic invariant set. Nowadays, however, unbound systems with transient chaotic behavior are well understood too [20] and show, in our opinion, notable simplifications with respect to their bound counterparts, as almost all trajectories spend a finite amount of time inside the system. Simple models such as the three-disk system—the equivalent of the famous billiards for closed systems—have been completely analyzed [21–23]; they demonstrated the existence of transient chaos for Hamiltonian dynamics.

Chaotic dynamics occurs as soon as homoclinic or heteroclinic intersections generate an overcountable infinite array of unstable periodic and quasiperiodic orbits. In a well-chosen Poincaré section, each of the periodic orbits is represented by an invariant set of points and the linearized neighborhood of each such points shows two eigendirections: the direction of the stable manifold, with a Lyapunov exponent $\lambda_s < 1$, and that of the unstable manifold, with $\lambda_u > 1$. The Liouville theorem enforces $\lambda_s \lambda_u = 1$. In order for chaotic scattering to occur, it is sufficient that the stable and the unstable invariant manifolds extend into the asymptotic regions defined by one or more coordinates increasing to infinity.

The closure of the set of all the unstable periodic orbits is the *invariant set*—the nonattracting chaotic set [24], as it is also called—of the chaotic scattering dynamics. This set has the properties of a fractal Cantor set and is characterized by exponential scaling laws, provided no islands of stable orbits are present [there are no Kol'mogorov-Arnol'd-Moser (KAM) tori]. This situation is called *hard chaos*, as opposed to *soft chaos* where stable islands coexist with unstable orbits. In the latter case, the invariant set has a different fractal character with nonexpontential scaling laws near KAM barriers.

It is the invariant set that determines the general properties of the particular dynamics at hand; hence it will be one of the main subjects of the present study. The bundle of stable manifolds emerging from the invariant set intersects the plane of possible initial conditions at infinity in an overcountable set of points. Each of these points represents the initial asymptotic conditions of a trajectory running eventually into a trapped orbit in an infinitely long time. (Similarly, the intersections of this plane with the unstable manifolds correspond to final asymptotic motions of trajectories emerging from the orbits of the nonattracting chaotic set.) As this set of intersections is connected to the invariant set by the Hamiltonian flow, it also displays a fractal structure closely related to that of the invariant set [24–26].

Chaotic scattering has thus the distinctive feature that the invariant set of the dynamics projects itself smoothly towards infinity through the Hamiltonian flow; therefore, it is represented "faithfully" in the asymptotic plane. As a consequence, we have access to the intricacies of the nonattracting chaotic set through several observables: the deflection function and the time delay function [23,24] as well as the cross sections [27]. We are thus able to analyze the structures that exist in the chaotic motion. In this paper, we will explore in details the hierarchic organization of the invariant set through the fractal set of singularities in the time delay function and perform a quantitative analysis of the chaos at hand using tools of the thermodynamic formalism [28–30].

In simple examples such as the three-disk problem and other systems, the validity of the above ideas have been shown [24,23]. Also, problems of relevance in atomic physics have been tackled, both time independent [31] and time dependent [32]. As soon as the potentials become more realistic, soft chaos seems to be the rule, even if islands of stability need not occupy a large portion of the phase space.

The rest of the paper is organized as follows. In Sec. II we derive the Hamiltonian most useful for our study. Section III describes the chaotic behavior in details, while in Sec. IV we analyze the fractal properties of the set of singularities by exploring its hierarchic organization. Section V discusses the structure of the invariant set and its manifolds, explaining the key features of the hierarchy observed. Section VI presents a global quantitative description based on the knowledge of the hierarchic structure using thermodynamic formalism. In Sec. VII we present conclusions and perspectives.

II. COLLISION HAMILTONIANS

In this section we sketch the derivation of the Hamiltonian one uses to couple the motion of the three atoms.

We restrict our treatment to a *collinear* configuration (Fig. 1) and consider only potential interactions of the central atom B with its two neighbors A and C, neglecting any interaction between A and C. Then a general Hamiltonian is of the form

$$\mathcal{H} = \frac{p_A^2}{2m_A} + \frac{p_B^2}{2m_B} + \frac{p_C^2}{2m_C} + V_{AB}\left(|r_A - r_B|\right) + V_{CB}\left(|r_C - r_B|\right). \quad (1)$$

By changing to relative coordinates $r_{l1} = |r_A - r_B|$ and $r_{l2} = |r_C - r_B|$, called *local* coordinates here, and their conjugate momenta p_{l1}, p_{l2} and by eliminating center-of-mass motion, we obtain the usual Hamiltonian with kinetic coupling of the two oscillators AB and BC:

$$\mathcal{H} = \frac{p_{l1}^2}{2m_{AB}} + \frac{p_{l2}^2}{2m_{CB}} - \frac{1}{m_B}p_{l1}\,p_{l2} + V_1(r_{l1}) + V_2(r_{l2}) \quad (2)$$

with m_{AB} and m_{CB} being reduced masses $[m_{IJ} = m_I m_J\,/\,(m_I + m_J)]$. We note that sometimes a potential coupling of the type $V_3(r_{l1}, r_{l2})$ is used together with the kinetic coupling; we shall not proceed in that direction here.

In the picture of local coordinates the motion of a representative point is *not* that of a point moving freely in potential hills and valleys, precisely because of the kinetic coupling. In order to restore the image of a pure potential motion, one changes from kinetic to potential couplings [33]. In the simpler case when the atoms A and C are identical (called the ABA or symmetric case), the kinetic coupling can be removed by introducing two new kinematic parameters

$$\cos\theta = \frac{1}{1 + m_B/m_A}, \quad (3)$$

$$m = \frac{m\,(m_A + m_B)}{2m_A + m_B}. \quad (4)$$

Oblique coordinates are then defined as

$$r_{o1} = r_{l1} + r_{l2}\cos\theta, \quad (5)$$
$$r_{o2} = r_{l2}\sin\theta \quad (6)$$

and the conjugate momenta p_{o1} and p_{o2} follow easily. The Hamiltonian in oblique coordinates, with potential coupling, becomes

$$\mathcal{H} = \frac{1}{2m}\left(p_{o1}^2 + p_{o2}^2\right) + V_1\left(r_{o1}, r_{o2}\right) + V_2\left(r_{o2}\right). \quad (7)$$

Now we go further towards a tractable Hamiltonian by specifying the potential V. As mentioned earlier, we

FIG. 1. Local coordinates r_{l1} and r_{l2} in a collinear configuration.

choose the most common model potential that has an acceptable asymptotic behavior, namely, the Morse potential,

$$V_{\text{Morse}}(r) = D\left(1 - e^{-a(r - R_e)}\right)^2. \quad (8)$$

This has been used for a long time to model interatomic interactions leading eventually to the formation of molecules. A large number of works have dealt with the classical and the quantum properties of coupled Morse Hamiltonians from various aspects [34–42]. In particular, several studies of the unbounded dynamics have discussed the role of unstable periodic orbits [43,44] and the invariant set [1,45–47]. The transition from regular to chaotic scattering has been treated analytically [48]. Most recent investigations use the complete theory of dynamical systems and chaotic scattering [4–6,8]; however, none of them gave a full-fledged hierarchic analysis of the system that will be presented here.

Let us now define reduced—dimensionless—quantities for the classical dynamics [49]. The following set of transformations introduces the relevant scaled quantities (distinguished by tildes from the unscaled ones):

$$\tilde{r} = ar, \quad (9)$$
$$\tilde{p} = p/\sqrt{2m_{AB}D}, \quad (10)$$
$$\tilde{t} = a\sqrt{2D/m_{AB}}\,t, \quad (11)$$
$$\tilde{\mathcal{H}} = \mathcal{H}/2D. \quad (12)$$

Since in the following we will use *reduced oblique coordinates* only, obtained from r_{o1} and r_{o2}, we apply the simple notation q_1, q_2 and p_1, p_2 for these new coordinates and their conjugate momenta, respectively. In these variables, the reduced Hamiltonian for the ABA case is

$$\tilde{\mathcal{H}} = \frac{\sin^2\theta}{2}\left(p_1^2 + p_2^2\right)$$
$$+ \frac{1}{2}\left\{1 - \exp\left[-\left(q_1 - q_2\cot\theta - \tilde{R}_e\right)\right]\right\}^2$$
$$+ \frac{1}{2}\left\{1 - \exp\left[-\left(q_2/\sin\theta - \tilde{R}_e\right)\right]\right\}^2. \quad (13)$$

We will use the above form of the Hamiltonian in the whole subsequent study. It contains only two independent parameters, namely, the *mass ratio* m_B/m_A and the quantity $\tilde{E} = E/D$, which is the energy measured in the units of the dissociation energy D of the ABA complex. (In other words, $\tilde{E}$ is just twice the total reduced energy $E/2D$ of the system.) They determine the overall topology of the flow in phase space. In these units, the motion is bounded for $0 < \tilde{E} < 1$ and unbounded otherwise. For $\tilde{E} > 2$, each of the separate AB oscillators is unbounded and the problem becomes meaningless.

III. CHAOS IN THE ABA SYSTEM

In this section we first summarize how permanent chaotic behavior appears at low energies ($\tilde{E} < 1$) and evolves into chaotic scattering (transient chaos) for $\tilde{E} > 1$. We discuss then how chaotic scattering trajectories may be analyzed and grouped into a hierarchic organi-
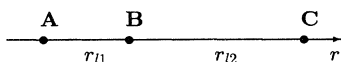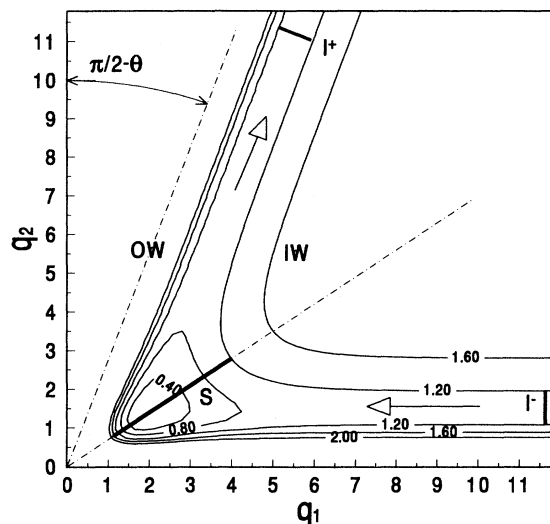
FIG. 2. Equipotentials, in *reduced oblique* coordinates of two coupled Morse potentials. Contour levels are in units of $\tilde{E} = E/D$. The equilibrium distance is $\tilde{R}_e = 1.46$. The symmetry axis of the figure $[q_1 = q_2 \tan(\theta/2)]$ is shown as a mixed line. The radial line corresponding to an angle θ is also drawn. S marks the symmetric stretch unstable periodic orbit ($\tilde{E} = 1.2$). I^- and I^+ suggest the infinitely distant periodic orbits with a freely oscillating AB diatom and a free fixed A atom at infinity. The labels OW and IW denote the outer and the inner walls of the potential, respectively (see Sec. IV B). The two arrows indicate the incoming and the outgoing channels for a *reactive* collision.

zation. We fix the mass ratio at $m_B/m_A = 2$ for the analysis; later, we will comment on to what extent our findings depend on that quantity. The shape of the potential surface for this mass ratio is shown in Fig. 2.

A. Bounded chaos

For $\tilde{E} < 1$ the phase space of the system is bounded since none of the coordinates can exceed a certain limit value. This bounded phase space is conveniently represented through an appropriate Poincaré section, e.g., by observing q_1 and p_1 at $q_2 = \tilde{R}_e \sin\theta$ and $p_2 > 0$. In this representation, each periodic orbit of the system appears as a finite set of discrete points, while quasiperiodic motion corresponds to closed curves (KAM tori). The chaotic orbits fill certain regions of the Poincaré surface.

At low energies ($\tilde{E} \gtrsim 0$), the behavior of the system is determined by two basic periodic orbits: the symmetric and the antisymmetric stretch of the ABA complex, just as in the case of two coupled harmonic oscillators. A generic orbit of the system is a quasiperiodic motion around one or both of the basic orbits [Fig. 3(a)]. Raising the energy, some of the tori break up, through bifurcations of periodic orbits, into smaller ones. Chaotic motion appears in their neighborhood and occupies larger and larger portions of the phase space with increasing energy [Fig. 3(b)]. At $\tilde{E} \simeq 0.5$ the symmetric stretch

becomes unstable and for $\tilde{E}$ close to 1, the phase portrait of the system consists of a stable island—located around the antisymmetric stretch orbit and surrounded by a KAM torus—immersed in a sea of chaotic motion [Fig. 3(c)]. Many studies have already described this scenario [35,37,47].
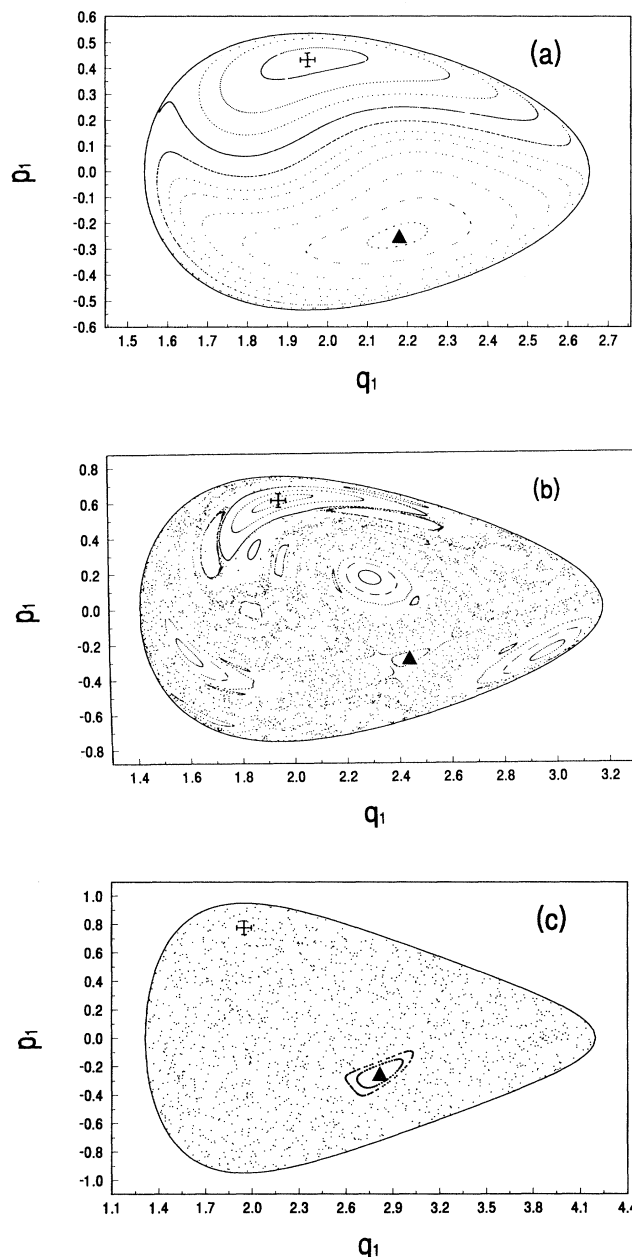

FIG. 3. Phase space portrait of the bounded ABA case ($\tilde{E} < 1$) for the potential of Fig. 2 at different energies in the Poincaré section $q_2 = \tilde{R}_e \sin\theta$. The cross and the triangle denote the two primary period-one orbits, the symmetric and the antisymmetric stretch, respectively. The energy values are $\tilde{E} = 0.2$ (a), 0.5 (b), and 0.8 (c). Please note the change of scale between the different phase space portraits.

B. Scattering orbits and transient chaos

The structure of the phase space changes drastically when passing through $\tilde{E} = 1$. At this energy, one of the A atoms may go arbitrarily far away from the remaining AB pair. Two new periodic orbits appear, characterized by the independent oscillatory behavior of the pair and the asymptotically free translation of the single atom. These orbits are located at an infinitely long distance from the center of the potential at $(q_1, q_2) = [\tilde{R}_e(1 + \cos\theta), \tilde{R}_e \sin\theta]$; for this reason we call them *infinitely distant orbits*. Becoming part of the phase space, they expand it to infinity along the lines $q_2 = \tilde{R}_e \sin\theta$ and $q_1 = \tilde{R}_e + q_2 \cot\theta$.

For $\tilde{E} > 1$ the unboundedness of the phase space results in the possibility of *scattering orbits* starting from an asymptotic free motion of an A atom toward the oscillating AB molecule (incoming part) and ending in the same or the other A atom running away from the remaining AB pair to infinity (outgoing part). If the outgoing part also runs along the incoming channel, then the collision is nonreactive (the two A atoms do not change roles), while an escape through the other channel means that the reaction has happened. The asymptotic parts are connected via an irregular behavior around the center of the potential. These scattering orbits are born from the bounded chaotic motion outside the stable island. Nevertheless, initial conditions located inside the island will result in bounded motion even for $\tilde{E} > 1$ as long as the island exists. This means that the new type of scattering orbits still coexist in phase space with the old bounded behavior inside the island. The island interior is not accessible for the unbounded orbits as they cannot cross the KAM barrier around the stable part of the phase space.

The new type of unbounded motion is an appearance of *transient chaos*, i.e., chaotic motion observed on a finite time scale. These scattering orbits show an extreme sensitivity to initial conditions due to the chaotic parts in them. The sensitivity is manifested in the fact that different quantities characterizing the scattering can vary very irregularly as a function of a (continuous) parameter in the initial conditions. For example, the time that a trajectory spends close to the center of the potential (scattering time or *time delay*) as a function of the initial condition parameter shows infinitely many singularities sitting on a *fractal* set characterized by self-similar properties. A study of the time delay function [23,50] allows one to obtain important quantities characterizing the chaotic set. We can also say that the singularities of the time delay function are a "fingerprint" of the chaotic set on the parameter axis.

The detailed properties of chaotic scattering depend on the mass ratio and the energy of the system. However, there are wide regions in this parameter space characterized by qualitatively similar scattering behavior. This can be understood by looking at the shape of the potential: it consists of two "channels" connected smoothly around the center of the potential (Fig. 2). The mass ratio sets the angle between the axes of the channels, through Eq. (3). This quantity, together with the energy,

will determine the rules how a trajectory coming in along one channel can follow its way into the other channel or return to the same one. These rules can be approximated by simple geometric arguments [18] or extracted directly from the behavior of the scattering orbits of the system. In Sec. IV, we will follow the latter approach in analyzing chaotic scattering in our model.

C. Time delay function

The hallmark of chaotic scattering in experimental or numerical data is the presence of singularities arranged in a fractal structure in the scattering functions [24,26]. To obtain, e.g., the time delay function $T(b)$, one takes a family of initial conditions with a variable parameter b for scattering (a line or a simple curve in configuration space or phase space) and measures the time T needed for the particle to leave the scattering region as a function of that parameter. The irregular behavior of this $T(b)$ function is caused by the existence of a nonattractive chaotic set in phase space. Each singularity of $T(b)$ corresponds to a bounded orbit, a member of the chaotic set: the scattering time is infinite for the exact initial condition with which we "hit" (asymptotically) the bounded orbit and can be arbitrarily large for nearby initial conditions. Since there is an infinite array of bounded orbits, there are infinitely many singularities in the time delay function and the self-similar ordering of the singularities reflects just the fractal structure of the chaotic set.

Now let us turn to the particular evaluation and analysis of the time delay function T in the ABA model. We consider the motion of a representative particle in the double Morse potential according to the Hamiltonian (13). The state of the ABA complex is represented by the position and the momentum of this particle. Our choice for the set of initial conditions is the following: (i) we fix the incoming translational momentum $p_1 < 0$ of the particle in the horizontal (q_1) channel at $q_1 = q_{\text{cut}} \gg \tilde{R}_e$ (we choose q_{cut} so that the potential term V_1 is less than 10^{-9} there so that we can neglect it) and (ii) change the starting phase of the oscillatory motion in q_2 as our parameter b in the initial conditions. For the sake of simplicity, we define this phase variable $\varphi \equiv b$ as if the oscillation were harmonic between the extreme points q_{max} and q_{min} allowed by the values of $\tilde{E}$ and p_1:

$$\varphi = \arccos\left(2\,\frac{q_2 - q_c}{q_{\text{max}} - q_{\text{min}}}\right), \tag{14}$$

where $q_c = (q_{\text{max}} + q_{\text{min}})/2$. As long as $\tilde{E}$ is not close to 2, where the oscillation becomes unbounded, φ can be connected by a smooth transformation to the phase of a Morse oscillator defined by the appropriate action and angle variables.

The trajectories started from these initial conditions will go into the central part of the potential and eventually leave it along one of the channels. To obtain the time delay function $T(\varphi)$, we simply measure the time needed for the trajectory to escape, i.e., to get farther from the origin $q_1 = q_2 = 0$ than the cutoff value q_{cut} in

one of the channels. Figure 4(a) shows this function for $\tilde{E} = 1.2$ and $p_1 = -0.4$. It contains smooth parts and singular peaks in a self-similar fashion. If we magnify a small part of the picture between two nearby peaks as in Fig. 4(b), we can see a picture that is similar to that in Fig. 4(a), i.e., it shows again smooth regions between the peaks arranged in a way that is similar to the overall pattern of peaks.

If we want to analyze this structure in details, a slightly different, discretized, version of the time delay function may be more appropriate. This modified function $X(\varphi)$ measures time by counting how many instances a given trajectory crosses a certain Poincaré surface of section. To obtain meaningful results, the Poincaré section must have the following property: escaping trajectories can cross it only a finite number of times and the number of crossings has to be an increasing function of the time a trajectory spends in the central region of the potential. The axes of the channels do not comply with the first requirement so we cannot use them for the purpose of

counting crossings. Instead, we choose as our Poincaré section the symmetry axis of the potential, which coincides with the symmetric stretch orbit in the configuration space. Indeed, this line is not crossed any more when a trajectory escapes in a channel, but all nearby orbits that turn back somewhere in that channel instead of escaping must cross it at least once more before they leave. In addition, this line is known to be a periodic orbit dividing surface [43], meaning that all other periodic orbits (except the infinitely distant ones) cross it. This also implies that scattering trajectories spending more time following a given periodic orbit will produce more crossings than other trajectories that escape sooner.

Based on the above considerations, we define the discrete time delay $X(\varphi)$ as the number of crossings of a trajectory with the symmetry axis [51]. The discrete time delay function for the previous values of $\tilde{E}$ and p_1 is shown in Fig. 5(a). Its similarity to Fig. 4(a) is obvious with the main difference that the smooth "valleys" between the singularities in $T(\varphi)$ are replaced with flat plateaus. That means that all trajectories chosen from the same valley produce the same number of crossings. It is also worth noting that the *parity* of this number tells us which channel the trajectories escape through, so we can conclude that all the trajectories from a given smooth valley use the same channel for exit.

In order to illustrate the dependence of the time delay function on the particular set of initial conditions, we show plots of the discrete version for two other choices. For Fig. 5(b), we set $p_1 = -0.05$ with the same energy as before, while Fig. 5(c) was made for $\tilde{E} = 1.4$ and $p_1 = -0.55$. If we compare these new plots and that in Fig. 5(a) to one another, they look very different globally. Yet a careful examination of their small-scale structure shows some basic similarities, as we explain in the next section.
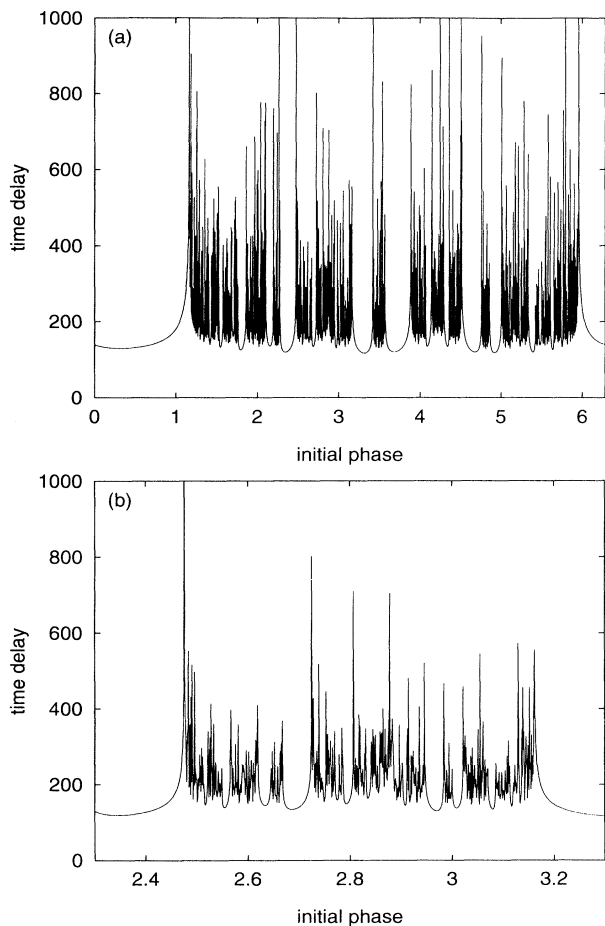

FIG. 4. Time delay function $T(\varphi)$ for initial conditions with (a) $\tilde{E} = 1.2$ and $p_1 = -0.4$ and (b) the blowup of the part $2.3 < \varphi < 3.3$. The initial phase φ is measured in radians and its range covers a whole cycle; the time delay is given in dimensionless units [see Eq. (11)].

IV. ANALYSIS OF THE DISCRETE TIME DELAY FUNCTION $X(\varphi)$

A. Hierarchic organization of orbits

The self-similar structure of the time delay function $X(\varphi)$ is built on the singularities that reflect the organization of the closed orbits of the chaotic set. Therefore, our analysis should concentrate on the irregular regions containing the peaks and disregard the smooth valleys between them. However, there are infinitely many smooth regions appearing on all length scales and, in addition, the smaller a valley, the larger the number of all similar-sized valleys in the time delay function. That means that we cannot get rid of them in one step; instead, we have to set up a *hierarchic* schedule of deleting them. As a first step we erase the widest smooth regions leaving behind a few blocks that we regard as sitting in the first level of the hierarchy. In a second step we magnify these blocks one by one and look for the most prominent valleys inside them. Those valleys are the ones to delete next in order to obtain a set of smaller blocks that

we put in the second level. In general, to construct one more level of the hierarchy we have to look into the elements of the previous level and divide them into smaller units by erasing the most prominent smooth regions inside. As a result of this procedure, we obtain better and better approximations of the set of the singularities by climbing higher and higher in the hierarchy. Since these singularities are connected to the chaotic set of the system, we gain important information on the organization of that object simply by examining the higher levels of the hierarchy.

At this point, two important questions arise: (i) which properties of the time delay function justify this hierarchic approach and (ii) how can we decide precisely which valleys to delete at a given level? The answers can be obtained by looking at the trajectories that sit in the main valleys. As we have noted earlier, trajectories of initial conditions inside a given valley produce the same number of crossings with the symmetry axis and consequently escape along the same channel. Since these orbits start from a connected part of the set of initial conditions and also appear as a single smooth part in the time delay function, they must be similar in their behaviors around the center of the potential, i.e., their central parts are qualitatively the same. In other words, a smooth transformation connects all the orbits of a single valley to one another and the variation in their (continuous) time delays mainly comes from the outgoing parts: they run "uphill" when leaving the system and the diverging edges of the valley in $T(\varphi)$ are produced by trajectories with more of their energy in vibration at the expense of translation in the asymptotic outgoing part. In contrast, two trajectories chosen from two different valleys show characteristic differences in their central parts even if they produce the same number of crossings. A few simple orbits chosen from various valleys of the time delay function are shown in Fig. 6.

By comparing trajectories representing different valleys, one can observe that, in general, the narrower a valley, the more complicated the corresponding orbits. In most cases, the complexity of orbits is reflected in the number of crossings characterizing the valley, i.e., the time delay is higher in narrower valleys. (There are, however, exceptions to this tendency, for a reason to be
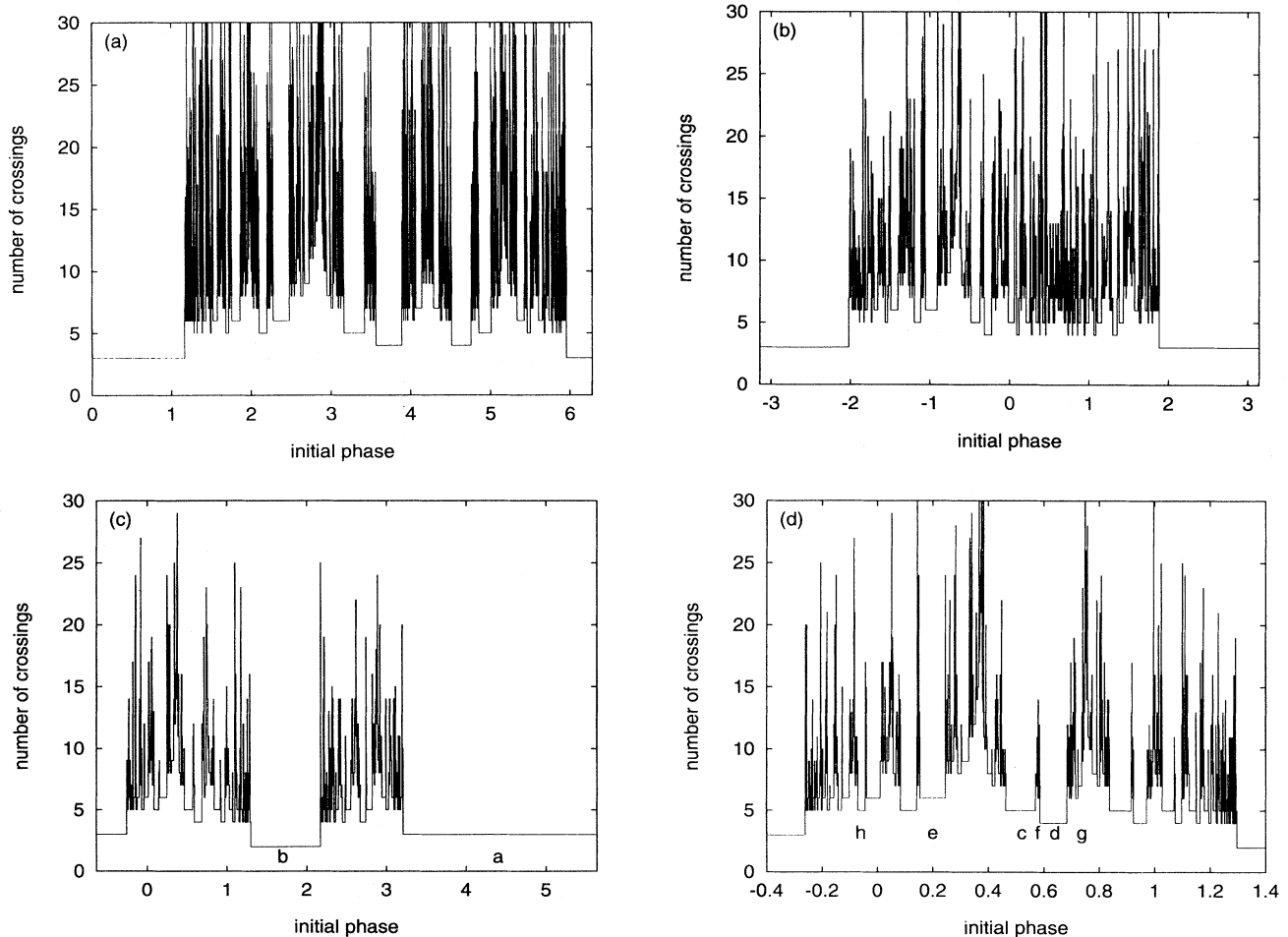

FIG. 5. Discrete time delay functions $X(\varphi)$ for initial conditions with (a) $\bar{E} = 1.2$, $p_1 = -0.4$; (b) $\bar{E} = 1.2$, $p_1 = -0.05$; (c) $\bar{E} = 1.4$, $p_1 = -0.55$; and (d) the blowup of the block on the left of Fig. 5(c). The labels a–h under the graphs in Figs. 5(c) and (d) identify the valleys that are represented by the corresponding typical trajectories in Figs. 6(a)–6(h), respectively.
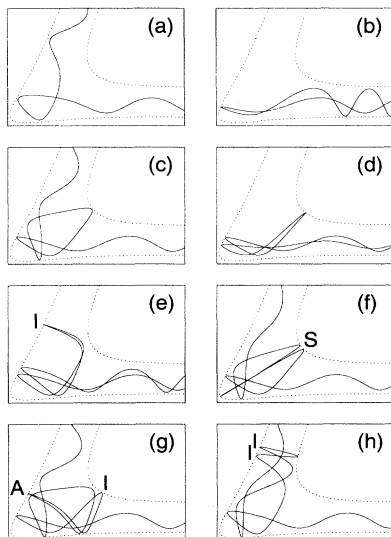
FIG. 6. Scattering trajectories representing various valleys of the time delay function in Figs. 5(c) and 5(d). All the windows show q_1 horizontally and q_2 vertically in the ranges $1 < q_1 < 8$ and $0.5 < q_2 < 6$; the dashed lines represent the edges of the constant energy surface at $\bar{E} = 1.4$. The trajectories come in from the right along the horizontal channel starting at $q_1 = q_{cut}$ with $p_1 = -0.55$ and with the following initial phases: $\varphi_a = 5.4$, $\varphi_b = 1.6$, $\varphi_c = 0.5$, $\varphi_d = 0.62$, $\varphi_e = 0.22$, $\varphi_f = 0.577$, $\varphi_g = 0.732$, and $\varphi_h = -0.06$. The orbits are characterized by the number of loops n performed in the central region. From those shown here (a) and (b) correspond to $n = 1$, (c) and (d) to $n = 2$, (e) and (f) to $n = 3$, and (g) and (h) to $n = 4$. Only the orbits (e)–(h) contain further loops between the entrance and exit ones; they are denoted by the labels S, I, and A according to their types (see text) next to their locations in the plots (the entrance and the exit loops are not marked). In some sense, the orbits (f)–(h) can be obtained from orbit (c) by inserting an S loop and loop sequences IA and II into its central part, respectively. Note that the discrete time delay is the same ($X = 5$) for orbits (c) and (h), although their central parts are different.

explained later.) The increasing complexity of the orbits in smaller valleys suggests that we should use this property in our analysis. For example, the widest valleys in Fig. 5(c) represent trajectories that perform just one simple loop in their central part with two or three crossings [Figs. 6(a) and 6(b)]. They are our natural candidates for deletion in the first step of our analyzing procedure. Indeed, they represent the simplest possible orbits in the system; the largest valleys from inside the two blocks contain trajectories performing at least one more loop and two more crossings before they exit [cf. Fig. 5(d) with Figs. 6(c)–6(h)].

In other words, all the trajectories from the blocks between the valleys just deleted at a certain level are longer and more complicated than those from the omitted valleys. Obviously, the simplest ones of these longer orbits sit in the most prominent valleys inside the blocks, so that these can identify the valleys to be deleted next.

That also means that the orbits of these newly selected valleys are just one "step" more complicated than the ones in the valleys deleted at the previous level. Looking at Fig. 6, one can see that the complexity of orbits grows in units of "loops": to obtain more complicated orbits from simpler ones, we can insert short self-crossing pieces into their central parts [compare, e.g., the orbits in Figs. 6(f)–6(h) to that in Fig. 6(c)]. In the sense used here, the term "loop" always refers to well-localized elements in the structure of an orbit with characteristic shapes, to be defined in the next paragraph, that can easily be identified in the graph of the orbit.

To be specific, the first or *entrance loop* is defined by the first self-crossing point when drawing the graph of a scattering trajectory; the last or *exit loop* can be found in a similar way as the first loop of the *time-reversed* orbit. These loops separate the central part of the trajectory from the incoming and the outgoing asymptotic motions. A careful examination of the orbits shows that the central part itself can be decomposed into loops by considering three different loop types.

(i) The S loop is a narrow orbit piece close to the symmetry axis like the one in the middle of the orbit in Fig. 6(f).

(ii) The I loops are located in the channels of the potential; a whole string of such loops is formed when the particle runs into a channel and turns back somewhere instead of escaping. The central part of the trajectory in Fig. 6(h) contains a string of two I loops.

(iii) The A loop runs across the symmetry axis and connects the two sides of the angle formed by the outer wall of the potential. The narrow loop in the orbit of Fig. 6(g), running parallel to the entrance loop and intercepting an I loop, is an example.

It is worth noting that, in a sense, these loops imitate the basic periodic orbits of the system. In fact, we chose the labels S, I, and A to underline the similarity of these loops to the symmetric stretch, the infinitely distant orbit, and the antisymmetric stretch, respectively.

The above definitions of loops also imply that some of the self-crossings in a trajectory are more important than others in the sense that they finish the creation of new loops of the types just described, while the other self-crossings are merely the results of overlaps between separate orbit pieces in the configuration space. For example, in the two-loop orbit of Fig. 6(c) the first and the last self-crossing give rise to the entrance and the exit loop, respectively, but in between there are four additional self-crossing points created by the overlap of these loops. In addition, there may also be self-crossings outside the central part involving the incoming or the outgoing asymptotic motion [see Fig. 6(c) with the outgoing part running over the two I loops or the nonreactive orbits of Figs. 6(b), 6(d), and 6(e) with an *infinite* number of self-crossings between the incoming and the outgoing asymptotic motions]; however, we never take these self-crossings into account when counting loops in a trajectory.

Using the loop types described above, a scattering trajectory can be considered as a sequence of loops con-

nected by simple orbit parts and the number of loops in the central part is a characteristics of the complexity of the trajectory [52]. Our detailed studies show that this tendency of orbit complexity increasing in terms of loops is general in the hierarchy of our system: the trajectories of the valleys at the next level of the hierarchy may be obtained from the trajectories deleted at the previous level by adding one more loop to their central parts. Since there are more than one type of loop to add, the number of all the valleys to be omitted at a certain level increases fast as we progress in the construction. It is precisely this hierarchic property of the orbits representing the valleys of $X(\varphi)$ that justifies the hierarchic approach in our analysis. In addition, it gives us a clue of how to identify the valleys to be deleted at the next level.

B. Ternary hiearchy

We performed the above analysis for the time delay functions shown in Figs. 5(a)–5(c). In Fig. 5(c), the two main blocks between the largest valleys (one-loop orbits with $X = 2$ or 3) form the first level of the hierarchy. One can observe that these blocks apparently have similar inner structures, which means that we can continue the refinement with just one of them (the reason for this similarity will be explained in Sec. V). The blowup of the block on the left [Fig. 5(d)] reveals many narrower valleys with four or five crossings; we have to choose those with the simplest orbits. It turns out that there are two valleys with two-loop orbits [see Figs. 6(c) and 6(d)], sitting on the two sides of the narrow spikelike part in the middle of the block, with time delays 4 and 5. By deleting them we create three smaller blocks for the second level of the hierarchy: the central "spike" and two larger regions. If we look into these new blocks, we again see similar patterns: many valleys with low numbers of crossings, but there are just two with the simplest orbits on the two sides of a central narrow spike with time delays $n_0 + 2$ and $n_0 + 3$, where n_0 denotes the height of the lower plateau next to the block outside. This rule for the division of blocks seems to apply at all levels available to our analysis yielding always three times as many new blocks at the new level as we had at the previous one. This procedure thus provides us with the successive refinements of a ternary hierarchy. Figure 7 shows the location (along the φ axis) of the blocks found at the first few levels.

The analysis revealed the same ternary structure in the cases of Figs. 5(a) and 5(b) in spite of the fact that they differ substantially at a first glance from Fig. 5(c). The most striking difference is that the valley with two crossings, together with a certain part of its neighborhood, is missing from both graphs; it looks as if the remaining parts were merged smoothly [the merging points being around $\varphi = 4.15$ and 0.6 in Figs. 5(a) and 5(b), respectively]. Actually, the missing part is smaller for Fig. 5(b), where the initial translational momentum is smaller; the reason for this will be clear in Sec. V. However, in spite of the differences at the basic level, these data apparently exhibit the same ternary organization as that of Fig. 5(c) up from the second level of the hierarchy: the refinement
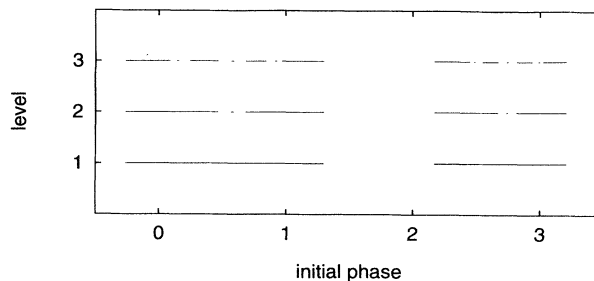

FIG. 7. The first three levels of the hierarchy for $\tilde{E} = 1.4$ and $p_1 = -0.55$ [cf. Fig. 5(c)]. The intervals at level n correspond to initial conditions that lead to trajectories performing at least n loops before their final exit loops. Each interval splits into three parts one level higher in accordance with the ternary hierarchy (the splitting of the smallest intervals at level 2 is invisible at this printing resolution). The lengths of these intervals will be used in Sec. VI as the basis of a quantitative description.

process splits every block into three at each new level.

When refining a block, we have to choose the right valleys to delete from a large (in principle, infinite) number of valleys with the same time delay value. The complexity of some orbits is apparently not reflected faithfully by their discrete time delays X. It turns out that all these orbits create additional I loops inside a channel by running into them but being unable to climb uphill high enough to escape: after a few vibrational cycles, they turn back toward the center [see Fig. 6(h)]. Actually, this is a consequence of the fact that the infinitely distant orbit sitting at the end of the channel does not cross the symmetry axis; thus the I loops approaching it do not produce crossings with the Poincaré section either. This represents a certain drawback of our choice of the symmetry axis as our Poincaré section. However, this choice, as we have seen, separates correctly along the φ axis the orbits with characteristically different central parts and does not mix them together even if they are given the same discrete time delay $X(\varphi)$. A comparison with the continuous time delay function $T(\varphi)$ can convince us in that respect. The distortion caused by this choice for the discretization remains just a small inconvenience.

The explanation of the ternary hierarchy can also be found by looking at the scattering orbits in details. To simplify our treatment, we will loosely talk about the "walls" of the potential (see Fig. 2) as if we had a hard-wall billiard system to describe some qualitative features of the orbits: we will refer to the inner wall inside the angle formed by the channel axes and to the two parts of the outer wall divided by the symmetry axis. Using these terms, we observe that all the trajectories start their central parts in qualitatively the same way (see Fig. 6): during the entrance loop, they run up to the part of the outer wall opposite the incoming channel and then they turn to the other part where they are deflected toward the inner potential wall that can send the orbits into either of the channels. Because of time reversal symmetry, the orbits exhibit the same pattern reversed in the exit loop. Con-
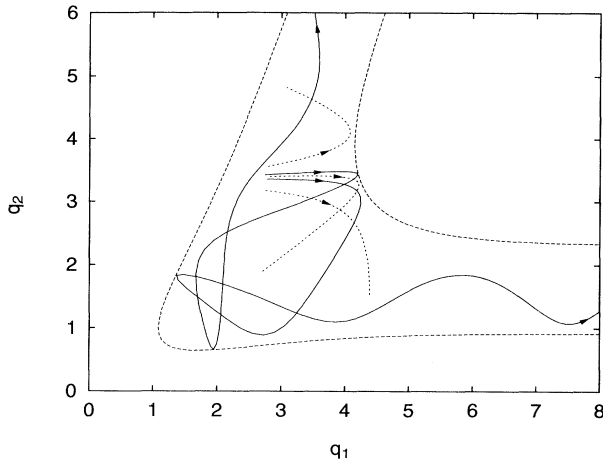
FIG. 8. Schematic plot illustrating the orbit patterns found when refining a block. The orbit parts shown here belong to five different trajectories taken from the same sixth-level block around $\varphi = 0.805$ in Fig. 5(d). We show the orbits after their sixth loops finished when they are still close to one another and all heading toward the inner potential wall. The separation occurs in the seventh loop: two of the trajectories start their exit loops (solid lines), while the other three can continue without escaping at this point (dashed lines). The two exit patterns correspond to the two valleys splitting the block into three. The dashed orbit parts represent the three possible continuation patterns (see text) and the three new blocks found at the seventh level of the hierarchy.

sequently, there are just *two ways* for an orbit heading towards the inner wall to escape: it can be deflected to either of the two parts of the outer wall because of the convex shape of the inner wall. Then the only possibility to leave as soon as possible is turning to the other part of the outer wall and finally run into the channel opposite that side (Fig. 8).

With these two simple routes for exit, the family of all orbits from a block at a given level of the hierarchy is divided into three smaller blocks containing trajectories that continue their wandering around the center. The orbits that do not escape at this point can therefore continue their course in the three ways sketched in Fig. 8: they either start an S loop around the symmetry axis or the inner wall deflects them towards one of the channels where they can perform further I and A loops. The role of the inner wall and its convex shape explains why the orbits can be thought of as organized in loops: the loops send the surviving trajectories back towards the inner wall where they again face the "choice" between the exit and the continuation patterns just described above. We can also see that the three ways of continuing an orbit are closely related to the three loop types introduced earlier and this fact can be used to construct a symbolic dynamics for the scattering orbits [53].

V. THE INVARIANT SET AND ITS MANIFOLDS

So far, we have based our analysis on some important characteristics of the scattering orbits. The origin

of these features can be best understood by looking at the properties of the nonattracting chaotic set responsible for the chaotic features of the scattering and the behavior of the stable and the unstable manifolds of the orbits belonging to the set. In particular, we will focus on the invariant manifolds of the two infinitely distant orbits since they are, in a sense, on the border between bounded and unbounded motion. The topological properties of these manifolds will help explain the organization of scattering orbits and the dependence of the time delay function on the choice of initial conditions.

We look at the above objects in the Poincaré surface of section, spanned by the coordinate q_s along the symmetry axis of the potential and the parallel momentum p_s when a trajectory crosses it. To avoid ambiguities, we should also require that the normal momentum be positive, but the symmetry of the potential allows us not to do so: starting two trajectories from a given point of the Poincaré section with opposite normal momenta yields a pair of orbits where one is just the mirror symetric image of the other. Since all the "right" crossings (i.e., with positive normal momenta) of the one orbit coincide on the section with all the "wrong" crossings of the other, our choice of registering all the crossings in a trajectory also yields the points representing its mirror symmetric pair. In other words, this choice identifies in the Poincaré section the orbits that are mirror symmetric images of each other.

A. Invariant set

The periodic orbits consist of discrete points in the section, so the invariant set appears as a set of points too, while the cross section of their invariant manifolds with this surface form smooth, but rather complicated, curves. There are two anomalously represented periodic orbits: the symmetric stretch orbit, which coincides in configuration space with the symmetry axis, is represented by the border of the constant energy surface, while the infinitely distant orbit does not produce crossings at all with the section. However, this does not cause any difficulty in our studies since all other trajectories approaching these orbits and their invariant manifolds are correctly registered in the Poincaré section.

First, we visualize the invariant set in the Poincaré section. It consists of all bounded orbits (i.e., those escaping neither forward nor backward in time) that are accessible for scattering trajectories. The invariant set can be best represented by plotting the points of a very long chaotic trajectory that does not escape. Although it is practically impossible to find an actual trajectory with this property because of the global instability of the nonattracting chaotic set, one can construct a so-called *saddle straddle trajectory*: a long sequence of tiny intervals, so that they cannot be distinguished from true points on a plot, sitting on the points of a true trajectory of the invariant set. The procedure is known as the proper interior maximum (PIM) triple method [54]. We start by choosing a sufficiently short segment I_0 in the Poincaré section that crosses (straddles) the stable mani-

fold of a bounded orbit and then we iterate it by following
the trajectories of its end points in the section. The dy-
namics will bring the iterates I_k $(k = 1, 2, 3, \ldots)$ of the
segment closer and closer to the invariant set along the
stable manifold while expanding them in the unstable di-
rection (the curvature of the iterates can be neglected if
the starting segment is short enough). When the length
of a certain iterate, say I_m, exceeds a preset limit value
δ, then we stop to refine it. We do this by starting trajec-
tories from a few points distributed in I_m and recording
their escape times. If we find a triple of starting points
with the property that the escape time is longer for the
middle point than for its neighbours (the fact that I_0
crosses a stable manifold ensures this), then we consider
this subsegment as the refined iterate I_m and follow its
images in the Poincaré section. The sequence of these
small intervals follows a true trajectory of the invariant
set, so by plotting it we obtain a good approximation of
that set.

With this method, we plotted in Fig. 9 the chaotic sets
for $\tilde{E} = 1.2$ and 1.4. One can clearly see the self-similar,
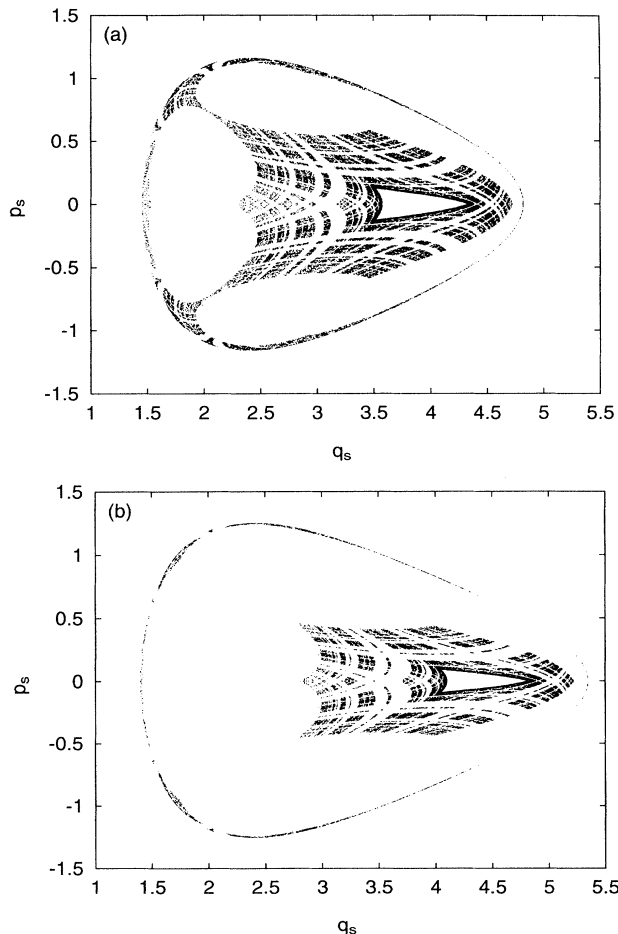fractal structure of the sets. Globally, they consist of

a large central part and a narrow border region, the for-
mer related to the channels with the infinitely distant or-
bits and the latter representing trajectory parts close to
the symmetric stretch orbit. In fact, this structure is re-
lated to the ternary organization: the central part can be
thought of as two identical parts, belonging to the two in-
finitely distant orbits, exactly coinciding in the Poincaré
section because of the symmetry of the potential. Glob-
ally, the ternary structure rests on these "three" parts
and its repetition in smaller and smaller scales can be
clearly observed in the central part. The border region
is very thin due to the strongly unstable nature of the
symmetric stretch, so the details of the structure are not
visible there.

For both energy values, there is a *stable island* around
the antisymmetric stretch orbit that appears in the plot
as an empty region with a triangular shape inside the
large domain. It looks empty because scattering trajec-
tories cannot enter this region. The triangular shape is
due to a nearby hyperbolic period-three orbit whose in-
variant manifolds, together with the remnants of broken
tori around the island, form a "cage" containing the is-
land as well as a very thin layer of chaotic trajectories
around it. This fact clearly illustrates the delicate inter-
play known as *squeezing* between a stable island around
a fixed point and a nearby period-three resonance [55]
found in generic Hamiltonian systems with a quadratic
nonlinearity. The presence of a stable island also im-
plies that there are some restrictions, called *pruning* [56]
in modern parlance, in ternary hierarchy due to the spe-
cial universal hierarchy of periodic orbits near KAM tori.
This means that certain scattering trajectories that were
otherwise allowed by the rules of the ternary organization
are forbidden; the cage that makes it difficult for scatter-
ing orbits to enter the immediate vicinity of the island
also makes it difficult to leave it once they are inside, so
there are no orbits spending just a short time close to
the island. Correspondingly, the ternary organization of
blocks in the time delay function breaks down in very
small regions containing trajectories that enter the cage.
In these regions, some blocks cannot be split into three
smaller blocks by the rules given in Sec. IV. This type
of pruning will remain as long as the stable island exists.
These flaws, however, are rather minor and affect only
the very high levels of the hierarchy, due to the "screen-
ing" effect produced by the nearby period-three orbit.
We checked for $\tilde{E} = 1.2$ that the first signs of this prun-
ing appear well above the $n = 50$ level, so the restrictions
are very subtle indeed.

Another interesting detail appears in the plot for $\tilde{E} =$
1.2 [Fig. 9(a)]: the central and the border regions are con-
nected by two thin filaments. As we will discuss later in
connection with the properties of the invariant manifolds,
they signal the presence of another source of pruning in
the system. In fact, the filaments are better considered
as the results of "collisions" of certain corners of the cen-
tral and the border regions, which makes certain types
of trajectories disappear. The fact that the filaments are
thin suggests that these restrictions are subtle too, i.e.,
the forbidden orbits are long and thus the pruning affects
the higher levels of the hierarchy only. For larger energies

FIG. 9. Chaotic set in the Poincaré section for (a) $\tilde{E} = 1.2$
and (b) $\tilde{E} = 1.4$ as approximated by long trajectories ob-
tained through the PIM triple method.

such as $\tilde{E} = 1.4$, the filaments disappear together with the restrictions they represent.

B. Stable and unstable manifolds

Now we explain the large scale structures of the invariant set and the time delay function by concentrating on the invariant manifolds of the infinitely distant orbits. The unstable manifold of a periodic orbit is generated by trajectories started slightly off the orbit in the unstable eigendirection of the linearized local dynamics. In the case of the infinitely distant orbits, that means we start trajectories in a channel far away from the origin with different vibration phases, as described in connec-
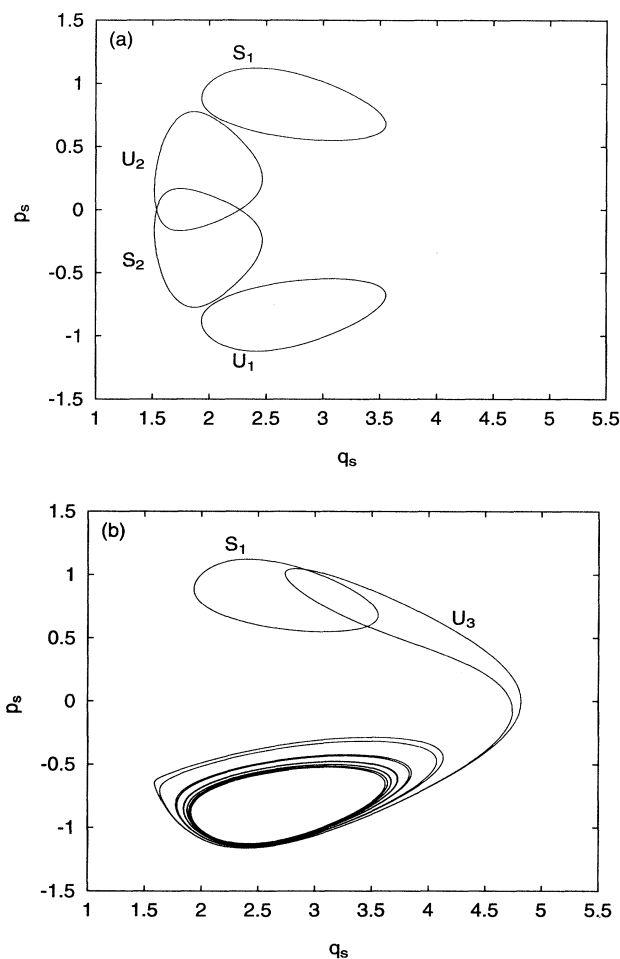

FIG. 10. (a) The first two branches of the stable and the unstable manifolds of the infinitely distant orbit in the Poincaré section for $\tilde{E} = 1.2$. (b) The unstable branch U_3 with S_1: it winds around U_1 many times due to trajectories that can almost escape after their second crossings with the symmetry axis. The stable branch S_3 (not shown to keep the figure clear) is the mirror image of U_3 with respect to the q_s axis. Together with S_1, S_2, U_1, and U_2, these curves set the frame for the invariant set in Fig. 9(a).

tion with the time delay function, but with almost vanishing incoming translational momentum. One such orbit produces discrete points in the section; when plotting the whole family of such orbits, these points draw up the unstable manifold as a set of curves. Since this family is parametrized by a phase variable, they yield a closed curve at the first crossing with the section that we call the principal or first branch U_1. Subsequent crossings of the trajectories yield the iterates U_2, U_3,... of the principal branch; we will refer to them as the second, third, etc., branches or iterates of the unstable manifold.

Figure 10 shows for $\tilde{E} = 1.2$ the first three branches of the unstable manifold of the infinitely distant orbit together with the branches S_1 and S_2 of its stable manifold. These latter branches were obtained by making use of the symmetry of the system: in reverse time the unstable manifolds turn into stable ones, which, combined with the mirror symmetry of the potential, means that the stable branches S_k are just the mirror symmetric images with respect to the q_s axis of the unstable branches U_k in the Poincaré section. We may observe that these curves—together with S_3, which is the mirror image of U_3—set a *frame* for the invariant set: the outer edges of the central and border parts of Fig. 9(a) coincide with pieces of these basic manifold curves and the corner points of the set are just the crossing points of the manifolds. It is also worth noticing that the first and the second branches are simple closed curves, but from the third iterates on, the curves become extremely complicated.

It can be checked that the scattering trajectories reach the Poincaré section *inside* the first unstable branch U_1, which also implies that they escape by entering into the domain of the stable branch S_1. Our initial conditions used in the construction of the time delay function can be represented by the locations of the first crossings of their trajectories: they form, therefore, a closed curve inside U_1. In order to understand the effect of the choice of initial conditions on the global structure of the time delay function, we present in Fig. 11 our initial conditions for $\tilde{E} = 1.2$ with the two choices $p_1 = -0.4$ and -0.05 and a few branches of the stable manifolds going through the first unstable branch. We realize that a small initial translational momentum leads to a curve close to the first unstable branch, as expected; in fact, U_1 practically coincides in Fig. 11 with the outer curve of initial conditions. Larger initial momenta cause this curve to shrink since large incoming speeds allow little vibration and thus variation in the initial condition by the phase variable.

Since the singularities of the time delay function appear at the crossings of the initial condition curve with the stable manifold branches, we can explain some of our earlier findings on the global appearance of this function. The "double" structure [see, e.g., the two blocks in Fig. 5(c) with similar inner properties] is simply caused by the fact that we used initial conditions that lie along the topological equivalent of a circle: they cross the stable branches twice. Indeed, we can see that the sequence of the corresponding valleys in the two main blocks of Fig. 5(c) are reversed as a consequence of this circular
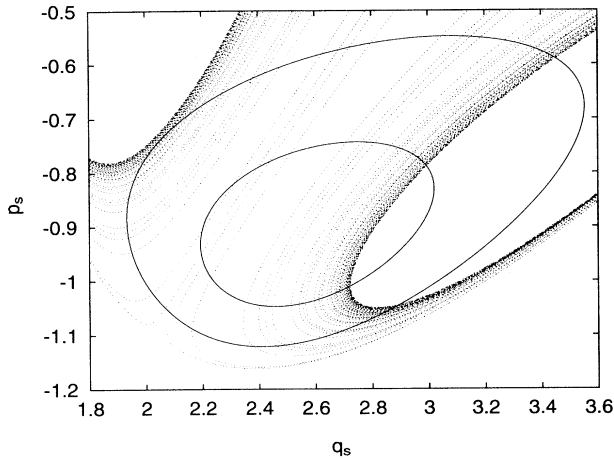
FIG. 11. Initial conditions used for Figs. 5(a) and 5(b), as represented in the Poincaré section by the first crossings of the trajectories (solid lines), together with branches S_2–S_6 of the stable manifold (dotted lines). The leftmost and rightmost stable manifold curves are pieces of S_2 and S_3, respectively. The inner closed curve corresponds to trajectories started with $p_1 = -0.4$, while the outer curve, practically coinciding with the principal unstable branch U_1, represents initial conditions with a small incoming translational momentum $p_1 = -0.05$.

topology. The shrinking of the initial condition curve with increasing initial translational momentum implies that for large incoming speed the curve cannot cross all the stable branches going through the first unstable branch, therefore some singularities will disappear from the time delay function. This gives the explanation for the "missing part" mentioned earlier and answers the question why it is larger in Fig. 5(a) than in Fig. 5(b).

Looking at the stable and the unstable branches can also be helpful in understanding particular properties of the scattering orbits. One can observe in Fig. 10(a) that the first stable and unstable branches do *not* cross, which means that there can be no scattering trajectory in the system having only one crossing with the symmetry axis of the potential. That explains why the scattering orbits start (and finish) their central parts with the loop described in Sec. IV. The branches U_2 and S_2, however, intersect each other, leading in turn to intersections between U_3 and S_1 (the dynamics maps U_k and S_k to U_{k+1} and S_{k-1}, respectively). This implies the existence of simple trajectories escaping after their third crossings [Fig. 6(a)]. The intersection points belong to *heteroclinic* one-loop orbits connecting the two infinitely distant orbits to each other (by "connecting" we mean that these orbits start their courses in one channel and finish it in the other with vanishing translational momentum). Similarly, crossings between U_2 and S_1 would imply that there exist one-loop *homoclinic* orbits, connecting an infinitely distant orbit to itself, and nearby scattering orbits with $X = 2$ [Fig. 6(b)]. In fact, as one can notice in Fig. 10(a), this is not the case for $\tilde{E} = 1.2$:

the first unstable branch does not cross the second stable branch. (This is the reason why we cannot see a plateau with $X = 2$ in the time delay function at this energy even for small incoming speeds.) They are, however, very close to that situation; thus a slight increase in the energy or the mass ratio can create crossings between these two branches (see, e.g., Fig. 3 in Ref. [46] for a mass ratio 2.5 at the same energy).

These observations can also shed light on the origin of the ternary organization. The basic homoclinic and heteroclinic trajectories between the infinitely distant orbits make it possible for a trajectory to leave along any of the two channels, no matter which channel it is in at a certain moment, thus creating the possibility for scattering trajectories to "choose" between the two exit patterns drawn in Fig. 8. This means that the ternary hierarchy is a consequence of the existence of both the one-loop homoclinic and heteroclinic connections between the infinitely distant orbits. The fact that the one-loop homoclinic orbits are missing for $\tilde{E} = 1.2$ also means the ternary hierarchy at this energy is slightly distorted: There must be blocks at higher levels that cannot be split into three because one of the exit loop possibilities is not allowed, so we encounter pruning again. The forbidden orbits turn out to be those that contain a long string of I loops. Since the source of this pruning is the missing homoclinic orbit (i.e., the missing crossings between S_2 and U_1 and similarly between S_1 and U_2), the forbidden scattering orbits are closely related to the thin filaments in Fig. 10(a): the filaments run between these manifold branches, so they can exist only as long as the homoclinic orbit does not. Thus we explained the nature of the pruning mentioned in Sec. V A in connection with the filaments. We also checked in the time delay function that the pruning is weak indeed: one has to look at higher levels ($n \geq 10$ in this case) to see its effect. This is a slightly stronger pruning than the one related to the stable island; however, since the branches U_1 and S_2 are close and will cross at higher energies, this form of pruning can disappear completely. This shows that the ternary hierarchy provides a very good approximate description of the organization of orbits in our cases.

VI. SCALING PROPERTIES AND THE FREE ENERGY FUNCTION

A. General formalism

The hierarchic analysis of the time delay function has provided us with successive approximations covering the fractal set of the singularities. These data can be used to extract important quantities characterizing the chaotic scattering process and the self-similar, or scaling, properties of its chaotic set. For this purpose, a quantity of central interest reflecting the hierarchic organization of chaotic scattering is the *free energy* $F(\beta)$. This function reflects the scaling behavior observed by following trajectories with increasing complexity around the scattering center [23], i.e., it is just based on the information obtained in our construction of the hierarchy.

The free energy is introduced in the spirit of the thermodynamic formalism of dynamical systems [28–30] via the relation

$$\sum_i \left(l_i^{(n)}\right)^\beta \sim e^{-\beta F(\beta)n}, \tag{15}$$

where β is an arbitrary real number and $n \gg 1$. $l_i^{(n)}$ denote the lengths of parameter intervals $I_i^{(n)}$ along the initial condition axis that cover the blocks sitting in the nth level of the hierarchy. It is an essential part of the definition of the intervals at level n that trajectories starting in the interior of a given interval should perform the same qualitative behavior for up to n steps, i.e., loops in our case, in the system. As we have seen, the nth-level blocks are defined by just this property. Figure 7 shows the intervals of the first few levels for the initial conditions used for Fig. 5(c).

It is worth briefly summarizing some basic features of the free energy function [23]. The graph $\beta F(\beta)$ vs β is monotonic increasing with a nonpositive second derivative. The values of $\beta F(\beta)$ taken at 1 and 0 immediately yield two basic characteristics of the scattering process: the *escape rate* and the *topological entropy*, respectively. The escape rate κ describes the exponential decay of the probability P_n for a scattering trajectory to survive through n loops in the scattering center: $P_n \sim e^{-\kappa n}$ (for large n). This probability is proportional to the sum of the lengths of all intervals at the nth level, thus κ also describes the exponential decay of the total interval length $\sum_i l_i^{(n)}$ with n. Thus

$$\kappa = F(1). \tag{16}$$

In the presence of nonexponential scalings (power law decays), this definition forces $\kappa = 0$. The topological entropy K_0 can be defined as the quantity characterizing the exponential growth of the number $N(n)$ of intervals $I_i^{(n)}$ with the level index n. Since the total number $N(n)$ of intervals is obtained from Eq. (15) at $\beta = 0$, we conclude that

$$K_0 = -(\beta F(\beta))|_{\beta=0}. \tag{17}$$

Note that K_0 also appears as the exponential growth rate of the number of *smooth* pieces (valleys) in the time delay function. For an unrestricted ternary hierarchy $K_0 = \ln 3$ and pruning makes it decrease due to the fact that some intervals disappear.

We will concentrate on other quantities as well that are, in our view, equally important characteristics of the scattering process. These are the average Lyapunov exponent $\bar\lambda$ of the dynamics on the chaotic invariant set and the fractal dimension D_0 of the set of singularities in the time delay function. They can be obtained as the derivative of $\beta F(\beta)$ taken at $\beta = 1$ and as the particular β value where the free energy vanishes, respectively, i.e., as

$$\bar\lambda = [\beta F(\beta)]'|_{\beta=1} \tag{18}$$

and

$$F(D_0) = 0. \tag{19}$$

It is worth noting that the fractal dimension of the nonattracting chaotic set itself is just $2D_0$ due to the Hamiltonian nature of the dynamics.

B. Results

We calculated the free energy from the discrete time delay functions shown in Figs. 5(a) and 5(c) by comparing the sums in Eq. (15) for two adjacent levels (4 and 5) of the hierarchy. The results are shown in Fig. 12; the most important quantities extracted from them are presented in Table I. We obtained $\ln 3$ for the topological entropy in both cases, suggesting a complete ternary hierarchy since the pruning effects mentioned earlier would only show up at n large enough. The value of κ can be used to estimate the average number $\bar n$ of loops that scattering trajectories taken from inside the two main blocks
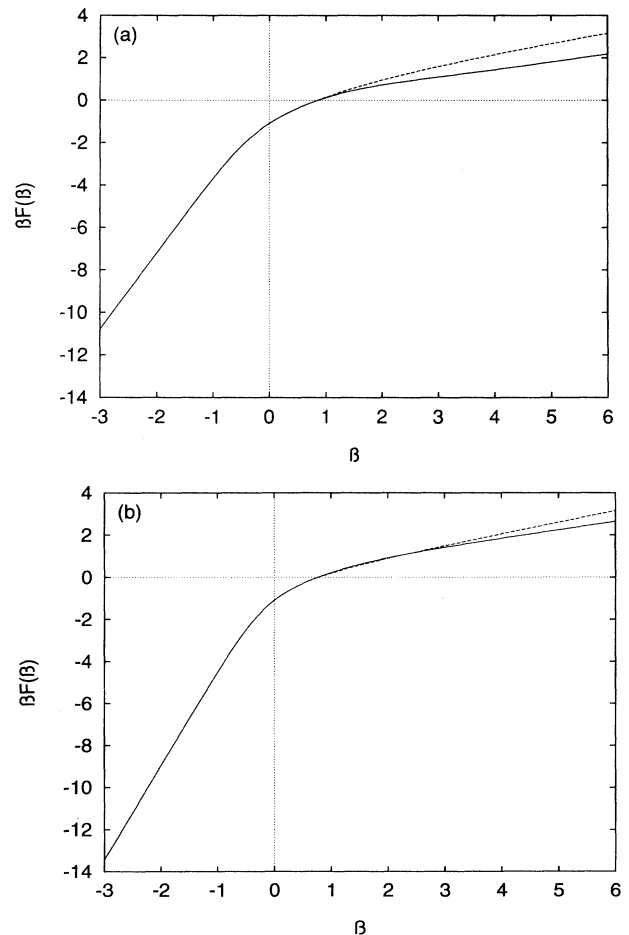

FIG. 12. Free energy function $\beta F(\beta)$ for (a) $\bar E = 1.2$ and (b) $\bar E = 1.4$ as calculated from the first five levels of the hierarchy (solid line). The dashed lines show the results obtained from the first four levels only; for $\beta > 1$ they differ substantially from the solid lines due to nonexponential scalings in the system.

TABLE I. Global quantitative characteristics of chaotic scattering in the double Morse potential. Values given below are those extracted from the data of Fig. 12. Uncertainties are of the order of 10%. See Sec. VI for further details and explanations.

Quantity	Value for	
	$\tilde{E} = 1.2$	$\tilde{E} = 1.4$
K_0	$\ln 3$	$\ln 3$
D_0	0.85	0.77
$\bar{\lambda}$	0.83	0.88
κ	0.12	0.22
$\bar{r}$	6.91	4.00

of the first level perform before the exit loop. Assuming a pure exponential distribution

$$\bar{n} = 1/(1 - e^{-\kappa}) \approx 1/\kappa \qquad (20)$$

for small κ. This yields $\bar{n} \approx 9$ and 5 for $\tilde{E} = 1.2$ and 1.4, respectively. The high values of $\bar{\lambda}$ signal strongly sensitive chaotic dynamics in the central part of the potential, while the fact that the fractal dimension D_0 is rather large in both cases is in complete agreement with the apparently dense structure of the chaotic sets.

The above quantities can also be combined to measure the global importance of chaos in the scattering process. The value $\bar{\lambda} > 0$ describes how far two typical nearby orbits will be repelled from each other during one loop. We can combine it with the average number of loops $1/\kappa$ a trajectory spends in the chaotic region to form the average repelling exponent $\bar{r}$ that scattering orbits will "feel":

$$\bar{r} = \bar{\lambda}/\kappa \qquad (21)$$

(see Table I). Large values of this quantity imply a dominant role of chaotic dynamics in the system as nearby incoming scattering trajectories are in general separated very far from one another during their lifetimes in the central region of the potential. This is in accordance with the fact that the difference $\bar{\lambda} - \kappa$ is equal to the Kol'mogorov-Sinai entropy K_1 [57] measuring the average loss rate of information in the system due to its chaoticity. On the other hand, the lack of chaos corresponds to the limit $\bar{r} \gtrsim 1$ (since $K_1 \geq 0$). This is the case, for example, when there is just one unstable bounded orbit in the system: then both $\bar{\lambda}$ and κ are equal to the logarithm of the unstable eigenvalue of that orbit.

It is worth noting that $\bar{r}$ is also related to the information dimension D_1 of the set of singularities by the formula $\bar{r} = 1/(1 - D_1)$. In general, D_1 is close to the fractal dimension D_0, so this connection supports our argument on the role of $\bar{r}$ as strong and weak chaotic features in scattering correspond to D_0 close to 1 (very irregular scattering functions) and 0 (smooth behavior), respectively. In addition, the approximate relationship $\bar{r} \approx 1/(1 - D_0)$ can be used to check the internal consistency of our results in Table I. One can see that the values listed there fulfill this condition within their numerical accuracy.

The convergence of this method, and thus the accuracy of our numerical results, can also be checked by evaluating the free energy from two lower levels (e.g., levels 3 and 4) of the hierarchy; if the new curve does not differ substantially from the previous one, then we are in the region of fast convergence and our quantitative results are reliable. Performing the comparison, the convergence seems clearly good for $\beta < 1$, but becomes increasingly worse for $\beta > 1$ (see Fig. 12). The reason for this is that there are parts in the chaotic set, and thus in the time delay function too, where the local scaling is not exponential. There are two sources for this anomalous scaling in our system: the long-distance tail of the Morse potential and the presence of KAM tori.

The Morse potential saturates exponentially [see Eq. (8)] to its "hilltop" value D for $r \to \infty$. One can show that the time period T_p of a single Morse oscillator with a total energy $E \lesssim D$ diverges as $T_p(E) \sim (D - E)^{-1/2}$, as opposed to the usual logarithmic divergence found for approaching a quadratic hilltop located at a finite distance from the equilibrium. This implies that the infinitely distant orbits of the double Morse potential are marginally stable and nearby orbits diverge from them slower than exponentially. Consequently, the size of the blocks containing orbits with more and more additional loops in one channel eventually decay according to a power law as we go higher in the hierarchy, indicating that the escape time distribution in the system has a power law tail. The scaling behavior found in Refs. [5] and [6] for similar situations also show this power law dependence.

This anomalous scaling behavior is, however, the consequence of our choice of the particular shape of the potential. There are more realistic potentials without this property (e.g., the already mentioned PQLEPS potentials) and choosing one of them eliminates this source of nonexponential scaling. On the other hand, the anomalous scalings caused by KAM tori are inherent in any generic smooth potential. Trajectories getting close to the edge of a stable island can stay for extremely long times in that neighborhood due to so-called cantori, i.e., the remnants of already broken former KAM curves. This implies a power law decay in the distribution of long escape times in the system [58,50]. Numerical experience also shows [50] that the "stickiness" of the islands leads to a (locally) distorted fractal structure of the chaotic set, which causes the fractal dimension D_0 of the set of singularities in the time delay function to be 1.

The presence of nonexponential scalings affects the values of the quantities we calculated earlier to characterize the system. Since the escape time distribution has a power law tail and the long time behavior is dominated by scattering trajectories exhibiting quasiperiodic motion in the vicinity of KAM tori for a long time, both the escape rate κ and the average Lyapunov exponent $\bar{\lambda}$ are expected to be zero, while the fractal dimension D_0 should approach 1, in the asymptotic limit $n \to \infty$. This implies that the free energy reaches the horizontal axis at $\beta = 1$ with zero slope. From its monotonic increase with never a positive second derivative it follows that $\beta F(\beta)$ has to be identically zero for any value $\beta \geq 1$. The tendency toward this behavior can be seen in Fig. 12 for

larger positive β values. Nevertheless, the results shown in Table I differ significantly from their asymptotic values. This may well be due to the fact that the anomalous scalings are connected to long orbits, so the free energy as approximated from the lower levels of the hierarchy available to our analysis is dominated by the contribution of shorter *hyperbolic* orbits with exponential scalings. Thus one expects a crossover at higher levels in the thermodynamic analysis from the hyperbolic type behavior to the asymptotic form of the free energy caused by the nonhyperbolic orbits.

This also implies that our results as presented here are still relevant, being the contributions of the hyperbolic part of the chaotic set. They describe the statistical properties of the system correctly as long as only not too long orbits are taken into account. Since in our case the effect of the stable island is largely screened by the nearby hyperbolic period-three orbit, the dominant nonhyperbolic contribution comes from the exponential tail of the Morse potential. This means that the time range in which our results are meaningful could be expanded considerably by choosing a more realistic form for the interatomic potential.

Finally, it is worth mentioning that other parts of the free energy can provide us with useful information too. For large negative β values the slope of the graph of $\beta F(\beta)$ tends to a constant, namely, the decay rate of the fastest shrinking blocks in the hierarchy. Similarly, the asymptotic slope of $\beta F(\beta)$ for $\beta \gg 1$ gives the slowest rate of shrinking in the system. In our case, the fastest decay is produced by refining the central narrow spike inside a block in each step of the hierarchic analysis. The spikes contain trajectories that approach the symmetric stretch orbit. Indeed, our numerical results show that the asymptotic slope of the graph for $\beta \ll -1$ coincides with the Lyapunov exponent of the symmetric stretch, telling us that this orbit is the most unstable one. For large positive β the asymptotic slope cannot be measured directly due to the lack of convergence there, but its tendency to move toward 0 is in complete agreement with the fact that marginally stable orbits are present in the system.

VII. DISCUSSION AND CONCLUSIONS

We have presented in this paper a thorough description of the chaotic scattering in two coupled Morse oscillators. Our central result is a hierarchic procedure to analyze the structure of the nonattractive chaotic set through looking at the singularity pattern of the time delay function and the organization of scattering orbits. We found that the set of scattering orbits is organized according to a ternary hierarchy, at least at the lower levels, for the particular parameter values taken in the study. This follows from a similar structure in the nonattracting chaotic set. This hierarchy is based on the number of loops trajectories perform in their central parts. By using the tools of the thermodynamic formalism, the hierarchic analysis also allowed a quantitative characterization of the most prominent global features of the scattering process.

Since the actual results may well depend on the values of the energy and the mass ratio considered as well as on the particular form of the potential, it is worth discussing to what extent these details may affect our findings. The basic characteristics of the hierarchy, the approximate ternary organization, rest on the *topological* properties of the double Morse potential—namely, two channels connected smoothly to a potential well—that are common in a large number of model potentials describing collinear $A + BC \leftrightarrow ABC \leftrightarrow AB + C$ type reactions. The origin of the ternary nature for the symmetric Morse case can be found in the three basic periodic orbits: the symmetric stretch in the center and the two infinitely distant orbits at the "end" of the channels.

The analogs of these orbits are present in other potentials, possibly modified in form, but playing the same roles in the dynamics. In a different potential with a similar topology, the infinitely distant orbits may be replaced by true hyperbolic orbits located at a finite distance from the center, but their main feature, "closing" the channels for bounded orbits, remains unchanged. Similarly, the symmetric stretch may be deformed to a smooth curve in asymmetric configurations without ceasing to be a periodic orbit dividing surface that can be used in counting crossings for scattering trajectories. Therefore, we expect that our hierarchic analysis, with appropriate modifications, could be carried out in the cases of more realistic model potentials and the ternary organization itself would show up in those systems for suitable choices of their parameters. Indeed, the analysis of the collinear HgI_2 system in Ref. [8] showed a ternary organization in the fully chaotic regime. However, it is clear that effects of endo- or exo-energicity are not taken into account in these studies, although they might drastically modify the influence of the one or the other infinitely distant periodic orbit. This work is still entirely to be done.

The global properties of the dynamics strongly depend on the mass ratio through the angle θ formed by the channels of the potential surface. In a symmetric ABA configuration, θ is the only relevant parameter in addition to the energy [59]. Geometric arguments [18] as well as other considerations [45] show that for $\theta \approx \pi/k$ ($k = 2, 3, 4, \ldots$) the scattering process is dominated by *one* simple orbit pattern with just k crossings thus leaving little room for chaotic behavior. In these cases the unstable branch U_k runs close to the principal stable branch S_1 (see Fig. 4 in Ref. [46] for $k = 3$). In other words, for these special angles one has either the homoclinic or the heteroclinic connection (for k even and odd, respectively) between the infinitely distant orbits, but not both, so the ternary structure cannot build up.

On the other hand, if the channel angle is in the middle of the range $[\pi/k, \pi/(k-1)]$, then both types of connection exist, with k and $k-1$ crossings, allowing a larger share of chaos and a ternary organization in the scattering. One can easily check that the mass ratio $m_B/m_A = 2$ considered in this paper is somewhere halfway between the $k = 2$ and 3 cases, so that the two basic one-loop orbits of Fig. 6 can appear. A noticeable consequence of this feature is that one can expect an important role played by chaos for such light-heavy-

light type reactions when the different masses are still of comparable size, since we are then between the $k = 2$ and 3 cases. This is also a robust region in the sense that a slight change in the mass ratio would not lead to a completely different behavior. In contrast, for heavy-light-heavy reactions, the larger the difference between the masses is, the more sensitive the dynamics becomes to even small changes in the mass ratio.

For a given mass ratio, the energy dependence of the global phase space structure is expected to be less dramatic, since the energy affects only the size of the domains of U_n and S_n around the locations prescribed by the mass ratio. If these locations allow the intersections needed for the ternary hierarchy (i.e., θ is not close to the specific angles mentioned above), then there exists a critical energy $\tilde{E}_c$, dependent on the mass ratio, so that above this value the basic homoclinic and heteroclinic connections are present. Then the ternary organization is complete (at least as far as KAM tori allow at the lower levels of the hierarchy) and raising the energy further changes only the structure of the immediate vicinity of the stable island. (From Fig. 9 it is clear that for a mass ratio of 2, at $\tilde{E} = 1.4$ we are definitely above the critical energy, while at $\tilde{E} = 1.2$ we are slightly below it.)

Above $\tilde{E}_c$ there can be no drastic changes in the ternary hierarchy as long as the principal stable and unstable branches do not intersect—a situation that is closely connected to the presence of a stable island around the antisymmetric stretch orbit. For a Morse potential, the stable island remains for energies up to the total dissociation limit $\tilde{E} = 2$ [36,46]; for other potentials, it might disappear at higher energies, leaving the question about the range of validity of the ternary hierarchy open. Below $\tilde{E}_c$, we can consider the phase space structure as one with a pruned ternary organization; the closer we are to the bounded case $\tilde{E} = 1$, the stronger the pruning becomes. The above considerations indicate that the ternary hierarchy plays a central role in the classical models of such reactions.

It is also worth discussing the implications of our findings on the hierarchic structure from the point of view of chemical reactivity studies. Although the precise values of the scattering functions, such as $T(\varphi)$ and $X(\varphi)$, have no physical significance for an actual experimental situation, there are various average quantities of interest that can be computed from these functions. As we have seen, the quantity $\bar{n} = 1/\kappa$, extracted from $X(\varphi)$, gives the average lifetime of scattering orbits in the central region of the potential in terms of the number of loops perfomed there. This number $\bar{n}$ can also be regarded as an *estimate* of the average *intermediate complex lifetime* for the reaction in the appropriate natural time unit $(2\pi/a)\sqrt{(m_{AB}/2D)}$, which is the duration of one vibration cycle in a Morse potential at low energies.

Another common subject in chemical kinetics is the repartition of reaction products in vibrational channels (or, equivalently, in translational energy) [60]. In order to handle this problem in our classical treatment, one could construct a different scattering function $S(\varphi)$, in an analogous way to $T(\varphi)$, measuring the outgoing asymptotic vibrational action S as a function of the initial phase

φ. This function would have exactly the same structure as that of $T(\varphi)$ with the obvious difference that at the singularities S remains finite (taking its maximum value allowed by the total energy) instead of diverging. One could then use this function to calculate global quantities such as the average action $\bar{S}$. In regular scattering cases that would mean evaluating an integral; e.g., for $\bar{S}$ it would read $(1/2\pi)\int_0^{2\pi} S(\varphi)\,d\varphi$.

For chaotic scattering, because of the overcountable set of singularities, this is not possible unless we use the hierarchic information. Then we can calculate the integrals within each smooth part (valley) separately and sum them up in the order that they appear in the hierarchy, starting from the lowest level. Having included the contribution of the first n levels, the terms still missing are those of the blocks of level $n+1$ and higher. Since the total length of these boxes is proportional to $e^{-\kappa n}$, our procedure would converge exponentially fast, assuming hyperbolic contributions only. The convergence is driven just by the escape rate κ that we learned from our analysis of the time delay function. Other important quantities can also be calculated along similar lines: as an example, to obtain reaction probabilities one just has to add up the lengths of all valleys with an odd discrete time delay X, in the order prescribed by the hierarchy [61].

This shows that the knowledge of the hierarchy makes extracting important average quantities possible. Therefore the hierarchic analysis could play a vital role in the study of other reaction types such as unimolecular decays when the system can be modeled by a two-dimensional potential. We expect that a similar analysis could be carried out in those cases: all one has to do is to choose a Poincaré section that unambiguously defines the level of complexity of a given trajectory and then rearrange the orbits into a hierarchy according to their complexities. However, this approach cannot be applied in its present form to more complicated problems, e.g., to two- or three-dimensional reaction models, while the phenomenon of chaotic scattering in itself is still expected to be useful in the understanding of their properties. So far, it is an open question how this analysis of chaotic scattering could be extended to systems with more than two degrees of freedom.

[1] I. Hamilton and P. J. Brumer, Chem. Phys. **82**, 1937 (1985).

[2] D. M. Wardlaw and R. A. Marcus, Adv. Chem. Phys. **70-1**, 231 (1988).

[3] E. Ott and T. Tél, Chaos **3**, 417 (1993).

[4] R. T. Skodje and M. J. Davis, J. Chem. Phys. **88**, 2429 (1988); Chem. Phys. Lett. **175**, 92 (1990); R. T. Skodje, J. Chem. Phys. **95**, 7234 (1991); B. B. Grayce, R. T. Skodje, and J. M. Hutson, *ibid.* **98**, 3929 (1993).

[5] K. Someda, R. Ramaswamy, and H. Naramura, J. Chem. Phys. **98**, 1156 (1993).

[6] A. Tiyapan and C. Jaffé, J. Chem. Phys. **99**, 2765 (1993).

[7] L. Bonnet, J. C. Rayez, and Ph. Halvick, J. Chem. Phys. **99**, 1771 (1993); see also J. D. Kress, R.B. Walker, E.F. Hayes, and Ph. Pendergast, *ibid.* **100**, 2728 (1994), where the numerous resonances of the partial cross sections are mentioned only in passing.

[8] I. Burghardt and P.Gaspard, J. Chem. Phys. **100**, 6395 (1994).

[9] J. I. Steinfeld, J. S. Francisco, and W. L. Hase, *Chemical Kinetics and Dynamics* (Prentice-Hall, Englewood Cliffs, NJ, 1989).

[10] M. S. Child, *Semi-classical Mechanics with Molecular Applications* (Oxford Science, Oxford, 1991).

[11] M. Boiron, M. Lombardi, and L. Wiesenfeld, Phys. Rev. A **50**, 1409 (1994).

[12] C.-Y. Yang *et al.*, J. Chem. Phys. **100**, 4917 (1994).

[13] M. S. Child, *Molecular Collision Theory* (Academic, London, 1974).

[14] D. T. Colbert and W. H. Miller, J. Chem. Phys. **96**, 1982 (1992).

[15] T. Ericson and T. Mayer-Kuckuk, Annu. Rev. Nucl. Sci. **16**, 183 (1966).

[16] U. Smilansky. in *Chaos and Quantum Physics*, 1991 Les Houches Lectures, Session LII, edited by M. J. Giannoni, A. Voros, and J. Zinn-Justin (North-Holland, Amsterdam, 1991), p. 371.

[17] H.J. Stöckmann and J. Stein, Phys. Rev. Lett. **64**, 2215 (1990); E. Dorn and U. Smilansky, *ibid.* **68**, 1255 (1992).

[18] Ph. Halvick and J. C. Rayez, Chem. Phys. **131**, 375 (1989).

[19] Fully 3D effects are not to be neglected completely in this reaction. However, the linearity of the intermediate CNO and the absence of CO products show that the collinear feature has its importance in the process.

[20] T. Tél, in *Experiemtal Study and Characterization of Chaos*, edited by Hao Bai-lin (World Scientific, Singapore, 1990), p. 149.

[21] B. Eckhardt, J. Phys. A **20**, 5971 (1987).

[22] P. Gaspard and S. A. Rice, J. Chem. Phys. **90**, 2225 (1989); **90**, 2242 (1989); **90**, 2255 (1989).

[23] Z. Kovács and T. Tél, Phys. Rev. Lett. **64**, 1617 (1990); T. Tél, Phys. Rev. A **44**, 1034 (1991).

[24] S. Bleher, E. Ott, and C. Grebogi, Phys. Rev. Lett. **63**, 919 (1989); S. Bleher, C. Grebogi, and E. Ott, Physica D **46**, 87 (1990).

[25] B. Eckhardt and C. Jung, J. Phys. A **19**, L829 (1986).

[26] C. Jung and H. J. Scholz, J. Phys. A **20**, 3607 (1987); **21**, 2301 (1988).

[27] C. Jung and T. Tél, J. Phys. A **24**, 2793 (1991).

[28] D. Ruelle, *Thermodynamic Formalism* (Addison-Wesley, Reading, MA, 1978).

[29] M. J. Feigenbaum, M. H. Jensen, and I. Procaccia, Phys. Rev. Lett. **56**, 1503 (1986).

[30] T. Bohr and D. Rand, Physica D **25**, 387 (1987).

[31] R. Blümel, in *Quantum Non-Integrability*, edited by Da Hsuan Feng and Jian-Min Yuan (World Scientific, Singapore, 1992), p. 397.

[32] L. Wiesenfeld, J. Phys. B **25**, 4373 (1992).

[33] F. T. Smith, J. Chem. Phys. **31**, 1352 (1959).

[34] C. Jaffé and P. Brumer, J. Chem. Phys. **73**, 5646 (1980).

[35] R. M. Hedges and W. P. Reinhardt, J. Chem. Phys **78**, 3964 (1983).

[36] T. Matsushita, A. Narita, and T. Terasaka, Chem. Phys. Lett. **95**, 129 (1983).

[37] T. Matsushita and M. Terasaka, Chem. Phys. Lett. **100**, 138 (1983).

[38] T. Terasaka and T. Matsushita, Phys. Rev. A **32**, 538 (1985).

[39] E. L. Sibert, W. P. Reinhardt, and J. T. Hynes, J. Chem. Phys. **77**, 3583 (1982).

[40] R. B. Shirts, Chem. Phys. **114**, 187 (1987).

[41] Lu Zi-Min, M. Vallières, Yuan Jian-Min, and J. F. Heagy, Phys. Rev. A **45**, 5512 (1992).

[42] G. A. Voth and R. A. Marcus, J. Phys. Chem. **89**, 2208 (1985).

[43] E. Pollak and P. Pechukas, J. Chem. Phys. **69**, 1218 (1978); M. S. Child and E. Pollak, *ibid.* **73**, 4365 (1980).

[44] E. Pollak and M. S. Child, J. Chem. Phys. **73**, 4373 (1980).

[45] Ch. Schlier, Chem. Phys. **105**, 361 (1986).

[46] M. Berblinger and Ch. Schlier, Chem. Phys. Lett. **145**, 299 (1988).

[47] M. Berblinger, E. Pollak, and Ch. Schlier, J. Chem. Phys. **88**, 5643 (1988).

[48] B.-P. Koch and B. Bruhn, J. Phys. A **25**, 3945 (1992); Chaos **3**, 443 (1993).

[49] If we were to make quantum calculations, this reduction of the Hamiltonian would not be allowed, as $\hbar$ sets an absolute scale that is not compatible with the scaling introduced here.

[50] Y. T. Lau, J. M. Finn, and E. Ott, Phys. Rev. Lett. **66**, 978 (1991).

[51] In principle, we should record only crossings that happen in the same direction in a Poincaré section; however, at this point we just use the section to measure the scattering time. An orbit that produces m points in our Poincaré section crosses it either $2m - 1$ or $2m$ times depending on the exit channel, so our simplification of counting crossings in both directions does not distort the scattering time data while it gives us a clear distinction between reactive and nonreactive orbits with odd and even X values, respectively.

[52] At this point there is an interesting connection to *knot theory* [see, e.g., F. Y. Wu, Rev. Mod. Phys. **64**, 1109 (1992) for a simple imtroduction]. We may imagine replicating the graph of the central part of the orbit on a simple closed string (a circle) by deforming it using string moves called the *Reidemeister moves*. Then the number n of loops in the trajectory as we defined it is equal to the number of type-I moves (simple twists) needed to replicate the central part on the string, provided all the twists we apply have the same direction with respect to the orientation (the analog of time) of the string. In this case n corresponds to a topological invariant, the *writhe*, of the string.

[53] Z. Kovács (unpublished).

[54] H. E. Nusse and J. Yorke, Physica D **36**, 137 (1989).

[55] J. P. van der Weele, Ph.D. thesis, University of Amsterdam, 1987; J. P. van der Weele, H. W. Capel, T. P. Valkering, and T. Post, Physica A **147**, 499 (1988).

[56] P. Cvitanović, G. Gunaratne, and I. Procaccia, Phys. Rev. A **38**, 1503 (1988).

[57] J.-P. Eckmann and D. Ruelle, Rev. Mod. Phys. **57**, 617 (1985); H. Kantz and P. Grassberger, Physica D **17**, 75 (1985).

[58] C. F. Karney, Physica D **8**, 360 (1983); J. D. Meiss and E. Ott, Phys. Rev. Lett. **55**, 2741 (1985); M. Ding, T. Bountis, and E. Ott, Phys. Lett. A **151**, 395 (1990); Y. Lai, C. Grebogi, R. Blümel, and M. Ding, Phys. Rev. A **45**, 8284 (1992); C. F. Hillermeier, R. Blümel, and U.

Smilansky, *ibid.* **45**, 3486 (1992).

[59] In the asymmetric case, the other mass ratio parameter $\alpha = [m_C (m_A + m_B) / m_A (m_C + m_B)]^{1/2}$ apparently plays a lesser role: it affects the relative width of the two channels. In the following, we will discuss only the role of θ in symmetric configurations.

[60] R.D. Levine and R.B. Bernstein, *Molecular Reaction Dynamics and Chemical Reactivity* (Oxford University Press, New York, 1987), Chap. 7.

[61] We note that the seeds of this approach to calculate reaction probabilities have appeared in Ref. [44], but without any reference to the underlying hierarchic structure.